Nanoscale

Dynamic Article Links

Cite this: *Nanoscale*, 2011, **3**, 4301

www.rsc.org/nanoscale

PAPER

Long-range linear elasticity and mechanical instability of self-scrolling binormal nanohelices under a uniaxial load†

L. Dai,[a] L. Zhang,*[b] L. X. Dong,‡[b] W. Z. Shen,*[c] X. B. Zhang,[d] Z. Z. Ye[d] and B. J. Nelson[b]

Received 20th June 2011, Accepted 9th August 2011
DOI: 10.1039/c1nr10650c

Mechanical properties of self-scrolling binormal nanohelices with a rectangular cross-section are investigated under uniaxial tensile and compressive loads using nanorobotic manipulation and Cosserat curve theory. Stretching experiments demonstrate that small-pitch nanohelices have an exceptionally large linear elasticity region and excellent mechanical stability, which are attributed to their structural flexibility based on an analytical model. In comparison between helices with a circular, square and rectangular cross-section, modeling results indicate that, while the binormal helical structure is stretched with a large strain, the stress on the material remains low. This is of particular significance for such applications as elastic components in micro-/nanoelectromechanical systems (MEMS/NEMS). The mechanical instability of a self-scrolling nanohelix under compressive load is also investigated, and the low critical load for buckling suggests that the self-scrolling nanohelices are more suitable for extension springs in MEMS/NEMS.

1. Introduction

Nanohelices can provide a wide range of enhanced functionalities for micro-/nanoelectromechanical systems (MEMS/NEMS)[1–3] due to their helical shape,[4,5] superelasticity,[6–8] piezoresistive and piezoelectric properties,[9–11] as well as other characteristics.[12] Recently, strain-induced self-scrolling nanohelices have attracted considerable attention due to their highly controllable fabrication method that combines bottom-up thin film growth with top-down lithographic patterning.[13–15] This fabrication technique can create hybrid 3-D structures composed of metal, dielectric, and polymeric materials as well as semiconductor heterostructures.[16–20] More recently, small-pitch SiGe/Si and SiGe/Si/Cr nanohelices have been obtained.[21,22]

For nanohelices to serve as components for MEMS/NEMS or nanomechanical devices, their mechanical properties must be well understood. The mechanical properties of nanohelices under tensile loading have been investigated for several different materials, including carbon,[6] ZnO,[7] Si_3N_4[8] and InGaAs/GaAs.[23] Their mechanical stretching behavior was modeled using classical elasticity theory and the Kirchhoff rod model assuming an inextensible and unshearable rod. One report on the mechanical instability of a nanohelix under a compressive load demonstrated a nonlinear response of a buckling carbon nanohelix with a circular cross-section.[24] Though it is common to synthesize nanohelices with non-circular cross-sectional shapes, *e.g.* binormal helices, using top-down or bottom-up approaches,[2,13,25,26] a systematic study of the mechanical properties of these types of nanohelices under a uniaxial load has not been conducted.

In this paper, nanorobotic manipulation is used to examine the mechanical properties of a small-pitch SiGe/Si/Cr nanohelix under tensile and compressive loads. An analytical model based on Cosserat curve theory[27–29] is developed to explore the mechanical properties of both normal and binormal nanohelices with a rectangular cross-section, which are compared to helices with a circular or square cross-section. A primary advantage of Cosserat curve theory is that it assumes the materials are extensible and shearable. Among the four different types of the cross-sectional shapes, the binormal helix shows the largest linear elasticity under axial deformation. By quantitatively analyzing uniaxial loading experiments and modeling, three regions are identified: the final helical shape and the critical tensile force that causes fracture, the critical compressive force that causes buckling, and the spring constant between these two critical loads.

[a]*School of Mathematics and Physics, Suzhou University of Science and Technology, Suzhou, 215011, P.R. China*
[b]*Institute of Robotics and Intelligent Systems, ETH Zurich, CH-8092 Zurich, Switzerland. E-mail: lizhang@ethz.ch*
[c]*Laboratory of Condensed Matter Spectroscopy and Opto-Electronic Physics, and Key Laboratory of Artificial Structures and Quantum Control (Ministry of Education), Department of Physics, Shanghai Jiao Tong University, Shanghai, 200240, P.R. China. E-mail: wzshen@sjtu.edu.cn*
[d]*State Key Laboratory of Silicon Materials, Department of Materials Science and Engineering, Zhejiang University, Hangzhou, 310027, P.R. China*

† Electronic supplementary information (ESI) available: Cosserat curve modeling for a nanohelix with a rectangular cross-section. See DOI: 10.1039/c1nr10650c

‡ Current address: Department of Electrical and Computer Engineering, Michigan State University, East Lansing, MI-48824, USA.

2. Results and discussion

2.1. Self-assembly of a nanohelix on an AFM tip for nanorobotic manipulation

Small-pitch nanohelices were fabricated based on self-scrolling ribbons composed of stacked SiGe/Si/Cr thin films, as shown in Fig. 1(a). Nanorobotic manipulation in an SEM was used to investigate the mechanical properties in which one end of the nanohelix is glued on a manipulator probe and the other end of the helix manipulated by an AFM tip (Fig. 1(b)). When the distance between the manipulator probe and the AFM tip is less than approximately 0.45 μm, the inner wall of the free end of a nanohelix is attracted to the AFM tip (Fig. 1(c) and (d)) mainly by electrostatic forces. If the nanohelix is pulled away from the AFM tip along its helical axis, it is initially stretched and then detaches from the AFM tip when the applied force is over *ca.* 17 nN (Fig. 1(e) and (f)). Attaching a nanohelix to an AFM tip was performed with varied misalignment angles. An example is shown in Fig. 1(g)–(k). The results show that the attachment of the nanohelix on the AFM tip does not require precise alignment. The nanohelix was then firmly clamped onto the AFM tip using electron beam induced deposition (EBID) for manipulation.

2.2. Nanohelices under tensile load

Fig. 2(a)–(d) show the reproducible sequential elastic deformation and recovery process of a SiGe/Si/Cr nanohelix under tensile loading and unloading along its helical axis. In the experiment, the helix was elongated more than 170% of its original length. It then spontaneously detached from the AFM tip due to the large tensile force, and no plastic deformation was observed.

Based on Cosserat curve theory,[30] an analytical model is developed to explore the mechanical behavior of the normal and binormal helices, as shown in Fig. 2(e) and (f). The modeling results show that the load F and the geometry parameters of the radius (a_0 for the undeformed helix and a for the deformed one), and pitch (b_0 for the undeformed helix and b for the deformed

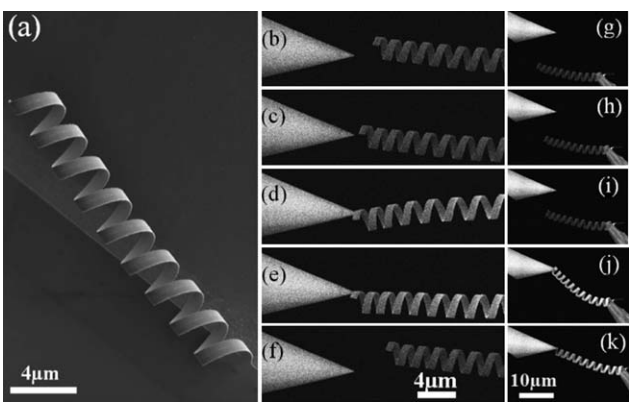

Fig. 1 (a) SEM images of an as-fabricated SiGe/Si/Cr nanohelix tethered on a Si substrate. (b–f) The nanohelix was attached to a manipulator probe and moved towards and away from the AFM tip. All frames have the same scale bar. (g–k) A sequence of frames shows the self-assembly of the misaligned nanohelix on the AFM tip. All frames have the same scale bar.

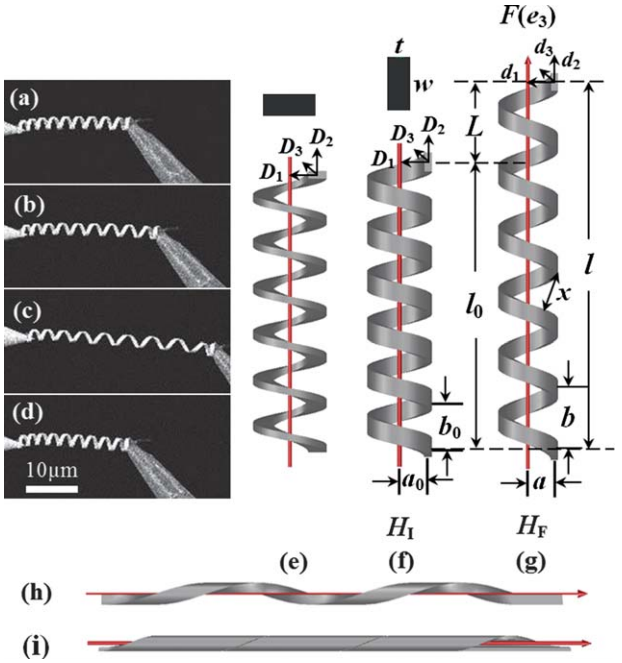

Fig. 2 (a–d) Tensile test of the nanohelix between the AFM cantilever and the tungsten probe. (e) Schematic illustration of a normal helix. (f) Schematic illustration of an unloaded binormal helix H_I with a rectangular cross-section. (g) Configuration of the binormal helix H_F after stretching by a tensile force F along its helical axis. (h and i) Configuration of a binormal helix after stretching to its limit.

one), shown in Fig. 2(f) and (g), are related to the intermediate Euler angles ϕ_0, θ_0, ψ_0 and ϕ, θ, ψ:

$$\left(\frac{1}{E_2}-\frac{1}{E_1}\right)\cos\theta\sin\theta F^2+\sin\theta F-C\dot{\psi}_0^2(\cos\theta-\cos\theta_0)\sin\theta$$

$$+EI_1[1-(\Delta-1)\delta_{i2}]\dot{\psi}_0^2(\sin\theta-\sin\theta_0)\cos\theta=0 \qquad (1)$$

$$a_0=\frac{\sin\theta_0}{\dot{\psi}_0},\ b_0=\frac{2\pi\cos\theta_0}{\dot{\psi}_0}, \qquad (2a)$$

$$a=\frac{1}{\dot{\psi}_0}\left[\left(\frac{F}{E_3}\cos\theta+1\right)-\frac{F}{E_1}\cos\theta\right]\sin\theta,$$

$$b=\frac{2\pi}{\dot{\psi}_0}\left[\frac{F}{E_1}\sin^2\theta+\left(\frac{F}{E_3}\cos\theta+1\right)\cos\theta\right] \qquad (2b)$$

where $\Delta \equiv I_2/I_1$, $i = 2$ (or $i = 1$) for a binormal (or normal) helix, δ_{i2} is the Kronecker delta, $E_1 = E_2 = KGtw$, $E_3 = Etw$, $A = EI_1$, $B = EI_2$, and $C = 4GI_1I_2/(I_1 + I_2)$ according to the scaled torsional stiffness.[31] The parameters w and t ($w > t$) are the width and the thickness of the curved nanobelt, respectively. K is the Timoshenko shear coefficient which is related to Poisson's ratio ν through $K = (5 + 5\nu)/(6 + 5\nu)$.[32] E and $G = E/2(1 + \nu)$ are the Young's and shear moduli of the nanobelt, respectively. $I_1 = w^3t/12$ and $I_2 = wt^3/12$ are the moments of inertia. (Details on modeling are available in the ESI†.)

The analytical model is compared to loading experiments of the SiGe/Si/Cr nanohelix, a typical binormal helix with

a rectangular cross-section shape.[33,34] Fig. 3(a) shows the dependence of the tensile load on the elongation of the nanohelix, in which the squares are from the experimental data and the solid curve is from the modeling. The relation between the applied force and elongation remains linear as the nanohelix is elongated to approximately 189%. In comparison with that of the nanohelices with a circular cross-section, *e.g.* 72% for the Si_3N_4 microcoil[8] and 15% for the carbon nanocoil,[6] the small-pitch self-scrolling nanohelix with a rectangular cross-section exhibits a much larger linear elastic range. The modeling result is from eqn (1) and (2) with parameters $a_0 = 1.5$ μm, $b_0 = 1.6$ μm, $t = 40$ nm, $w = 0.8$ μm, effective turns $N = 9$, $E = 140$ GPa, $\nu_{SiGe} = \nu_{Si} = 0.27$, and $\nu_{Cr} = 0.21$.[35,36] The modeling results agree with experiments well, which imply that the Cosserat curve model can also be used to analyze binormal helices under uniaxial load. Following the linear elastic domain of the nanohelix, a larger load is required to extend the nanohelix into a taut configuration. The nonlinear relationship between the elongation and the load shows that there is a huge change of the strain in this domain. The modeling results also indicate that the linear elasticity region of the nanohelices is significantly influenced by the cross-sectional shape of the helix. Fig. 3(b) shows the dependence of the tensile load on elongation for helices with four different cross-sectional shapes, *i.e.* rectangle (normal and binormal), square and circle, from eqn (1) and (2). We assume that, except for the cross-sectional shape, the four types of helices have the same parameters as those of the fabricated SiGe/Si/Cr nanohelix, including the area of the cross-section, the radius, the pitch, the number of turns, and the material parameters. The plot shows different linear regions of load *versus* elongation (solid line) for those four types of helices: the binormal helix possesses the largest elasticity linear region of *ca.* 220%, while the normal helix has the least of *ca.* 10%. The linear elasticity regions for the helix

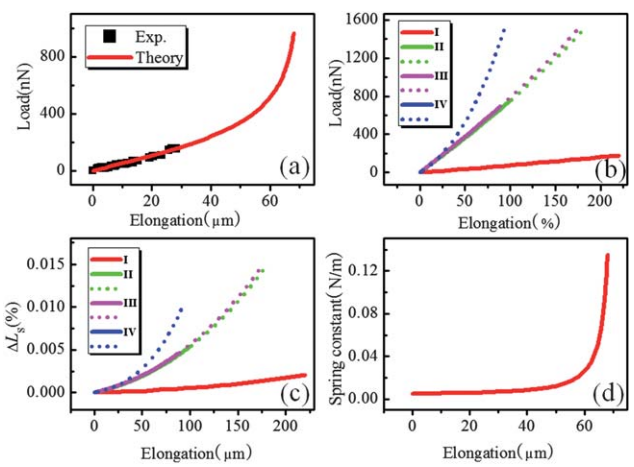

Fig. 3 (a) Experimental data of tensile load in the low-strain regime (squares) and theoretical calculation (solid curve) of load in the entire stretching region. (The experimental error, considered in the square, is attributed to the uncertainty in the position of the nanohelix.) (b) Tensile load and (c) relative materials stretch *versus* elongation for four types of helices with different shapes of the cross-section: (I) rectangle (binormal helix), (II) circle, (III) square and (IV) rectangle (normal helix). (d) Theoretical calculation of the spring constant *versus* elongation in the entire stretching region of the SiGe/Si/Cr nanohelix.

with a circle-shaped cross-section and a square-shaped cross-section are similar, *ca.* 100% and *ca.* 87%, respectively. The varied linear elasticity region of helices with different cross-sectional shapes is mainly due to the difference in the material stretch (λ) of the helical ribbon or the helical filament under axial load. This can also be deduced by using the Cosserat curve model. The material stretch of a helix is given by

$$\lambda = \sqrt{\frac{F^2}{E_1^2}\sin^2\theta + \left(\frac{F}{E_3}\cos\theta + 1\right)^2} \tag{3}$$

Fig. 3(c) illustrates the dependence of the relative stretch ($\Delta L_S = \lambda - 1$) of the four types of helices on their elongation in which the binormal helix presents the smallest ΔL_S for the same elongation. The results imply that for helices under axial loading situation the binormal helix is most stable under large deformation compared to the other three types of helices. Furthermore, unlike a helix with a circular cross-section, two different helical shapes of a stretched binormal helix can occur under a large tensile load if both ends are fixed. As shown in Fig. 2(g), x is defined as the distance between two adjacent exposed edges of the nanobelt along its width direction, which is expressed by

$$x = \frac{2ab}{\sqrt{(2a)^2 + (b/2)^2}} - w. \tag{4}$$

When a binormal helix is stretched to its limit, the sides of the ribbon are almost parallel to the helical axis and the relationship

$$w^2 + (2\pi a)^2 + b^2 = 2\left[(2a)^2 + \left(\frac{b}{2} + \frac{w\sqrt{(2a)^2 + (b/2)^2}}{4a}\right)^2\right] \tag{5}$$

is satisfied. If the geometry parameters from eqn (5) lead to $x \geq 0$ in eqn (4), the binormal helix can reach its elongation limit (Fig. 2(h)), similar to that of a helix with a circular cross-section. A tubular-like shape forms[25] as the edges of the adjacent turns of the helical ribbon touch each other ($x \leq 0$), as shown in Fig. 2(i). The final helical state of the binormal helix can be derived from eqn (4) before fracture. In combination with eqn (1) and (2), one can determine that the SiGe/Si/Cr nanohelix retains a helical shape with a radius of 0.4 μm, and a pitch of 9.2 μm when stretched to its limit by a critical force of 979 nN. The corresponding relative stretch is 0.02%, much smaller than 0.30% for Si_3N_4 and 2.30% for carbon nanocoils with a circular cross-section.[28]

The spring constant for the normal and binormal helices can be calculated by:

$$k = -\frac{P_1 P_4}{N(P_3 P_4 + P_2)} \tag{6}$$

where

$$P_1 \equiv \left[\dot{\psi}/2\pi\right] \Big/ \left[1 + 2F\cos\theta\left(\frac{1}{E_3} - \frac{1}{E_1}\right)\right],$$

$$P_2 \equiv 2\left(\frac{1}{E_3} - \frac{1}{E_1}\right)\cos\theta\sin\theta F + \sin\theta,$$

$$P_3 \equiv -\left[\frac{1}{E_1}+\left(\frac{1}{E_3}-\frac{1}{E_1}\right)\cos^2\theta\right]\Big/\left[1+2F\cos\theta\left(\frac{1}{E_3}-\frac{1}{E_1}\right)\right],$$

$$P_4 \equiv \left(\frac{1}{E_3}-\frac{1}{E_1}\right)\frac{1-2\cos^2\theta}{\sin\theta}F^2-\frac{\cos\theta}{\sin\theta}F$$
$$+\dot{\psi}_0^2\{EI_1[1-(\Delta-1)\delta_{i2}]-C\}\frac{1-2\cos^2\theta}{\sin\theta}$$
$$-EI_1[1-(\Delta-1)\delta_{i2}]\dot{\psi}_0^2\sin\theta-C\dot{\psi}_0^2\cos\theta_0\frac{\cos\theta}{\sin\theta} \quad (7)$$

Fig. 3(d) presents the spring constant of the SiGe/Si/Cr nanohelix in the entire stretching region before fracture, obtained using eqn (6) and (7). In the linear elasticity region of the SiGe/Si/Cr nanohelix, the spring constant k is a constant and the average value is calculated as 5.5×10^{-3} N m^{-1}, which agrees with experimental data. In the high strain regime of the helix, the spring constant increases rapidly and eventually reaches a critical value of 1.4×10^{-1} N m^{-1} before fracture.

2.3. Nanohelices under compressive load

One application of nanohelices is as a wirelessly controlled probe for micromanipulation in fluid. For example, helical swimming microrobots such as artificial bacterial flagella (ABF) have been realized using a corkscrew motion for propulsion.[37,38] Investigating the mechanical instability of this helical micromachine is important in understanding its performance limits as a manipulation tool. An axial compressive force was applied on a SiGe/Si/Cr nanohelix using a manipulator probe to investigate the buckling of the nanohelix, as shown in Fig. 4(a)–(d). The results indicate that initially the nanohelix is compressed along its helical axis, however, when the compressive force reaches approximately 6 nN, the helical structure becomes mechanically unstable and buckling occurs, as shown in Fig. 4(b). The buckling becomes more severe as the applied force increases by translating the tungsten probe towards the AFM tip, as shown in Fig. 4(c) and (d). In contrast to a helix under a tensile force, in which the spring constant of the helix increases with a large stretch, the spring constant of a helix under compression shows the opposite effect in the buckling regime. The diagram in Fig. 5(a) shows the dependence of the compressive load on the deformation of the SiGe/Si/Cr nanohelix in which experimental results are marked by squares and the modeling results by the solid line. The deformation of the helix under compression, measured from the SEM images, is defined as the shortened length of the helix between its fixed end on the manipulator probe and the AFM tip. When the compressive force (F) is smaller than the critical load F_{cr} (dashed line), the relation between the deformation and the compressive load can be predicted using the Cosserat curve model. To estimate the critical load F_{cr} of the SiGe/Si/Cr nanohelix, we define the corresponding length as l_{cr} with the decrease of Δ_{cr}, and ξ the pitch angle, as schematically shown in Fig. 4(e) and (f). The critical load of a buckling slender body is given by:[39]

$$F_{cr} = \frac{\pi^2\alpha_0}{l_{cr}^2} \quad (8)$$

For a helical body, the bending rigidity can be obtained by

$$\alpha_0 = \frac{\sin\xi}{\frac{1+\sin^2\xi}{2EI_2}+\frac{1-\sin^2\xi}{2GJ}}$$

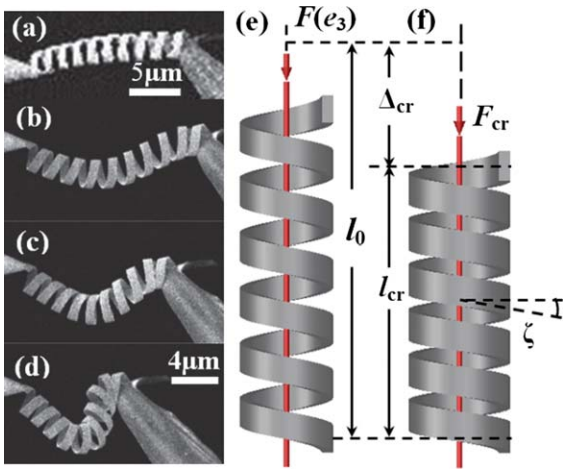

Fig. 4 (a–d) A series of SEM images showing the deformation of the nanohelix under an increasing compressive load. (a) Axial compression with a force smaller than the F_{cr}. (b–d) Buckling of the nanohelix. All frames have the same scale bar. (e) Illustration of a binormal helix under an axial compression in which $F < F_{cr}$. (f) Illustration of a binormal helix under the critical load F_{cr}.

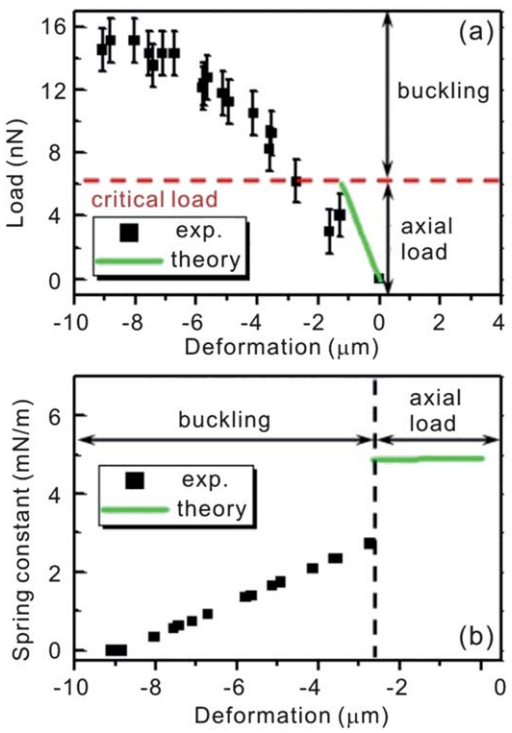

Fig. 5 Experimental data (squares) and theoretical calculation (solid line) of (a) load and (b) spring constant *versus* deformation in the axial compression and buckling regime. (The experimental error is attributed to the uncertainty in the position of the nanohelix. In (b), it is considered in the square.)

and $l_{cr} = l_0 - \Delta_{cr}$ with

$$\Delta_{cr} = \frac{2\pi Na_0^3}{\sqrt{1-\sin^2\xi}}\left(\frac{\sin^2\xi}{EI_2} + \frac{1-\sin^2\xi}{GJ}\right)F_{cr}.$$

Since the pitch angle ξ is small $\sin\xi = l_{cr}/s_0$ with the total length of the helical ribbon $s_0 = 2\pi Na_0$, and $\sin^2\xi = 0$. Eqn (8) can then be rewritten as:

$$F_{cr} = \frac{\pi}{Na_0\left(\frac{1}{EI_2}+\frac{1}{GJ}\right)\left(1-\frac{2\pi Na_0^3}{GJ}F_{cr}\right)} \quad (9)$$

And the critical value of F_{cr} is given by:

$$F_{cr} = \frac{l_0\left(\frac{1}{EI_2}+\frac{1}{GJ}\right) - \sqrt{l_0^2 I_2^2 - 4\pi\left(\frac{1}{EI_2}+\frac{1}{GJ}\right)\frac{2\pi Na_0^3}{GJ}}}{2\left(\frac{1}{EI_2}+\frac{1}{GJ}\right)\frac{2\pi Na_0^3}{GJ}} \quad (10)$$

Using eqn (10) and the geometry parameters of the SiGe/Si/Cr nanohelix, the critical load $F_{cr} = 6$ nN is determined, which is consistent with experimental results. When the compressive load is larger than F_{cr}, the nanospring is mechanically unstable and buckling occurs. Fig. 5(b) shows the spring constant of the nanohelix in the compression regime. The spring constant, derived from eqn (6), remains a constant in the axial compression domain (solid line), and decreases linearly from 3×10^{-3} N m^{-1} to approximately zero with increasing load in the post-buckling regime (squares). The reason for the linear decrease of the spring constant in the post-buckling region is unclear, but a similar phenomenon was also reported in a carbon nanocoil when an axial compressive force is loaded.[24] The nanospring recovers to its initial shape from the post-buckling state when the compressive load is removed.

3. Conclusions

We have investigated the mechanical properties of nanohelices with a rectangular cross-section under tensile and compressive loads. Based on the Cosserat curve theory, a comprehensive model for normal and binormal helices is proposed. The model and experiments reveal that a binormal helix with a rectangular cross-section, such as a self-scrolling nanohelix, has a large linear elasticity regime and is more mechanically stable due to a lower stretch of materials under large axial deformation. A tubular-like shape can also be formed from binormal helices under a large stretch. Finally, the mechanical instability of a self-scrolling nanohelix under compressive load is investigated. With knowledge of the mechanical properties of self-scrolling nanohelices, this work provides a reference for further design and fabrication optimization of normal and binormal helices for potential applications in MEMS/NEMS and as tools for micromanipulation.

4. Experimental section

4.1. Fabrication

Small-pitch SiGe/Si/Cr nanohelices were fabricated by the following procedure. The SiGe/Si hetero-film with a thickness of 11/8 nm was grown by ultrahigh vacuum chemical vapor deposition (UHV-CVD) on a Si(001) substrate. The Cr layer with a thickness of 21 nm was deposited by e-beam evaporation. Subsequently the small-pitch nanohelix was formed by wet chemical etching in an alkaline solution (3.7% NH_4OH). The fabrication of small-pitch nanohelices with pitch angles less than 10° can be achieved in a highly controllable fashion, when the edge effect dominates the coiling process of these ribbon-like patterned thin films.[21,22] Finally, the samples were dried in a supercritical point dryer to eliminate the capillary force.

4.2. Nanorobotic manipulation

To perform mechanical property characterization experiments, a SiGe/Si/Cr nanohelix with a radius of 1.5 μm, a pitch of 1.6 μm, a number of turns of 10 and a nanobelt width of 0.8 μm was assembled between a tungsten probe (Picoprobe, T-4-10-1 mm) and an AFM tip (Mikromasch, CSC38/Ti–Pt, stiffness 0.03 N m^{-1}). Controlled by the manipulator, the tungsten probe was prepared by dipping the tip into a silver conductive tape and then used to break and pick up the as-fabricated nanohelix from its tethered end. The free end of the nanohelix was then transported close to the AFM tip. When the distance between the manipulator probe and the AFM tip is sufficiently small, the inner wall of the nanohelix free end is attracted to the AFM tip. For the study of mechanical properties after the self-assembly step, the free end of the helix was clamped onto the AFM tip using electron-beam-induced deposition (EBID).[4] The manipulation processes were performed by translating the manipulator tungsten probe toward and away from the AFM tip, hence, uniaxial load was applied and the applied force was measured by the deflection of the AFM cantilever.

Acknowledgements

We thank B. H. Zhao (Zhejiang University) for technical support of the UHV-CVD facility, the FIRST lab of ETH Zurich for technical support of microfabrication, and X. J. Huang (Donghua University) for the simulated three-dimensional helices diagram. Some SiGe/Si bilayer samples were prepared at the Paul Scherrer Institute; the authors thank Dr J. Gobrecht and Dr D. Grutzmacher for their support. Funding for this research was partially provided by open funding (grant no. SKL 2009-4) of the State Key Laboratory of Zhejiang University, P. R. China, Sino-Swiss Science and Technology Cooperation (SSSTC, grant no. EG 08-092009) and Natural Science Foundation of China (grant no. 10734020).

References

1 P. X. Gao, Y. Ding, W. J. Mai, W. L. Hughes, C. S. Lao and Z. L. Wang, *Science*, 2005, **309**, 1700.
2 B. A. Korgel, *Science*, 2005, **309**, 1683.
3 Y. G. Sun and J. A. Rogers, *J. Mater. Chem.*, 2007, **17**, 832.
4 L. X. Dong, L. Zhang, B. E. Kratochvil, K. Y. Shou and B. J. Nelson, *J. Microelectromech. Syst.*, 2009, **18**, 1047.
5 L. Zhang, J. J. Abbott, L. X. Dong, K. E. Peyer, B. E. Kratochvil, H. X. Zhang, C. Bergeles and B. J. Nelson, *Nano Lett.*, 2009, **9**, 3663.
6 X. Q. Chen, S. L. Zhang, D. A. Dikin, W. Q. Ding, R. S. Ruoff, L. J. Pan and Y. Nakayama, *Nano Lett.*, 2003, **3**, 1299.
7 P. X. Gao, W. J. Mai and Z. L. Wang, *Nano Lett.*, 2006, **6**, 2536.
8 C. B. Cao, H. L. Du, Y. J. Xu, H. S. Zhu, T. H. Zhang and R. Yang, *Adv. Mater.*, 2008, **20**, 1738.

9 K. Hjort, J. Soderkvist and J. Schweitz, *J. Micromech. Microeng.*, 1994, **4**, 1.
10 Y. W. Hsu, S. S. Lu and P. Z. Chang, *J. Appl. Phys.*, 1999, **85**, 333.
11 G. Hwang, H. Hashimoto, D. J. Bell, L. X. Dong, B. J. Nelson and S. Schon, *Nano Lett.*, 2009, **9**, 554.
12 Y. Furuya, T. Hashishin, H. Iwanaga, S. Motojima and Y. Hishikawa, *Carbon*, 2004, **42**, 331.
13 V. Y. Prinz, V. A. Seleznev, A. K. Gutakovsky, A. V. Chehovskiy, V. V. Preobrazhenskii, M. A. Putyato and T. A. Gavrilova, *Phys. E.*, 2000, **6**, 828.
14 O. G. Schmidt and K. Eberl, *Nature*, 2001, **410**, 168.
15 A. Cho, *Science*, 2006, **313**, 164.
16 O. G. Schmidt, N. Schmarje, C. Deneke, C. Muller and N. Y. Jin-Phillipp, *Adv. Mater.*, 2001, **13**, 756.
17 L. Zhang, E. Deckhardt, A. Weber, C. Schonenberger and D. Grutzmacher, *Nanotechnology*, 2005, **16**, 655.
18 R. Songmuang, C. Deneke and O. G. Schmidt, *Appl. Phys. Lett.*, 2006, **89**, 223109.
19 Y. F. Mei, D. J. Thurmer, C. Deneke, S. Kiravittaya, Y. F. Chen, A. Dadgar, F. Bertram, B. Bastek, A. Krost, J. Christen, T. Reindl, M. Stoffel, E. Coric and O. G. Schmidt, *ACS Nano*, 2009, **3**, 1663.
20 V. Luchnikov, O. Sydorenko and M. Stamm, *Adv. Mater.*, 2005, **17**, 1177.
21 L. Zhang, L. X. Dong, D. J. Bell, B. J. Nelson, C. Schoenenberger and D. Gruetzmacher, *Microelectron. Eng.*, 2006, **83**, 1237–1240.
22 L. Zhang, E. Ruh, D. Grutzmacher, L. X. Dong, D. J. Bell, B. J. Nelson and C. Schonenberger, *Nano Lett.*, 2006, **6**, 1311–1317.
23 D. J. Bell, L. X. Dong, B. J. Nelson, M. Golling, L. Zhang and D. Grutzmacher, *Nano Lett.*, 2006, **6**, 725–729.
24 M. A. Poggi, J. S. Boyles and L. A. Bottomley, *Nano Lett.*, 2004, **4**, 1009–1016.
25 R. Oda, I. Huc, M. Schmutz, S. J. Candau and F. C. MacKintosh, *Nature*, 1999, **399**, 566–569.
26 E. D. Sone, E. R. Zubarev and S. I. Stupp, *Angew. Chem., Int. Ed.*, 2002, **41**, 1705–1709.
27 A. B. Whitman and C. N. Desilva, *J. Elasticity*, 1974, **4**, 265–280.
28 L. Dai and W. Z. Shen, *Nanotechnology*, 2009, **20**, 465707.
29 L. Dai and W. Z. Shen, *J. Appl. Phys.*, 2009, **106**, 114314.
30 E. Cosserat and F. Cosserat, *Theorie des corps deformables*, Hermann, Paris, 1909.
31 Z. C. Zhou, P. Y. Lai and B. Joos, *Phys. Rev. E: Stat., Nonlinear, Soft Matter Phys.*, 2005, **71**, 052801.
32 A. E. H. Love, *Treatise on the Mathematical Theory of Elasticity*, Cambridge University Press, Cambridge, 1982.
33 A. Goriely and P. Shipman, *Phys. Rev. E: Stat. Phys., Plasmas, Fluids, Relat. Interdiscip. Top.*, 2000, **61**, 4508.
34 A. F. da Fonseca, C. P. Malta and D. S. Galvao, *Nanotechnology*, 2006, **17**, 5620.
35 W. A. Fate, *J. Appl. Phys.*, 1975, **46**, 2375.
36 L. Zhang, L. X. Dong and B. J. Nelson, *Appl. Phys. Lett.*, 2008, **92**, 143110.
37 L. Zhang, J. J. Abbott, L. X. Dong, B. E. Kratochvil, D. Bell and B. J. Nelson, *Appl. Phys. Lett.*, 2009, **94**, 064107.
38 L. Zhang, K. E. Peyer and B. J. Nelson, *Lab Chip*, 2010, **10**, 2203–2215.
39 S. Timoshenko and J. Gere, *Theory of Elastic Stability*, McGraw-Hill, New York, 1961.